Precision Agriculture (2025) 26:71
https://doi.org/10.1007/s11119-025-10262-0

High-resolution sensing of maize nitrogen status through under-canopy RGB imaging using a mobile platform

Zafer Bestas[1] · Harold M. van Es[1] · William D. Philpot[2] · Kent Cavender-Bares[3] · David G. Rossiter[1,4]

Accepted: 17 June 2025

Abstract

Purpose Digital technologies have significantly improved nitrogen (N) fertilizer optimization in precision agriculture. A limitation of existing crop N detection approaches is that they primarily focus on above-canopy spectral measurements, overlooking the potential insights from lower canopy levels, which may more accurately reflect N stress through spectral reflectance associated with differential pigment expression.

Methods This study introduces high-resolution Red, Green, and Blue (RGB) under-canopy imaging of maize (*Zea mays L.*) to assess in-season N fertilizer application at high spatial resolution using a 30 frames/sec acquisition rate. Utilizing a purpose-built field robot, developed specifically for this study and equipped with a digital RGB camera, field trials were conducted across Minnesota and New York with varying N rates. Analysis using multiple thresholding methods for the (R-B)/(R+B) index from images captured during day and night revealed a strong correlation between under-canopy images and applied N rates.

Results R^2 values reached up to 0.78 in daytime and 0.92 under nighttime conditions. Semivariogram analysis indicated a range of influence of less than 6 m and showed that N stress spatial patterns are most pronounced with low N levels. Maps were generated based on 6-m field sections to represent field variability of N stress.

Conclusion These findings suggest that high-resolution under-canopy RGB imaging is a viable, lowcost method for detecting maize N status with very high spatial resolution, offering a new perspective for precision agriculture.

Keywords Precision agriculture · Nitrogen management · Under-canopy imaging · RGB · Robotic field sensing

Introduction

Nitrogen (N) is a crucial nutrient for the growth of field crops. N Fertilizer constitutes an average of 36% of a farmer's operating costs for maize production. In recent years, agriculture has been the single largest source of N compounds entering the environment in the United States, accounting for 73% of nitrous oxide emissions, 84% of ammonia emissions,

Extended author information available on the last page of the article

Published online: 23 July 2025

and 54% of nitrate losses (Ribaudo et al. 2011). Notably, excessive crop nitrogen application above the economic optimum N rate (EONR) leads to groundwater contamination, environmental pollution that degrades coastal aquatic ecosystems, and contributes to global warming through nitrous oxide emissions. A component of an efficient farming strategy is the precise detection and characterization of plant deficiencies followed by the proper corrective application of fertilizers. But precision nitrogen management in crop production remains a "wicked problem" due to challenges to estimate the EONR that are complicated by variable site-specific production conditions (esp. weather) and the need to balance producer and environmental risks (Correndo et al., 2021; van Es et al., 2007a, 2007b).

Modern precision agriculture techniques may achieve positive financial and environmental results (Alivernini et al., 2018; Pasuquin et al., 2014). Image-based sensing tools for crop biomass and canopy characteristics are widely available (Wang et al., 2022; Xue et al., 2004; Zhang et al., 2020) and generally employ satellite, aircraft, or more recently unmanned aerial vehicles (UAVs) (Cai et al., 2019; Campolo et al., 2022; Fan et al., 2022; Gilliot et al., 2021; Sharifi, 2020). Alternatively, dynamic modeling technologies can provide N fertilizer recommendations accounting for the seasonal conditions using climate data and field-specific information on crop and soil management (e.g., Adapt-N; Melkonian et al., 2017). Combining field-based sensing with dynamic models may provide complementary information, especially for the purpose of mid-season N applications. Therefore, utilizing an ensemble strategy can enhance economic and environmental benefits (Abit et al., 2018; Griffin et al., 2018).

Spatially variable rate application is typically based on sensors to assess N requirements (Shaver et al., 2010; Stamatiadis et al., 2010; Tremblay et al., 2009; Xiong et al., 2018). Frequent and high-resolution data acquisition and correct interpretation for accurate and precise application of fertilizer-N can thereby lead to improved N use efficiency, which is especially desirable in maize and some cereal crops that require high N amounts for optimum yields (Chen & Wang, 2022; Davies et al., 2020; Ogunboye et al., 2020; Prey & Schmidhalter, 2019). Current satellite images are generally low resolution for spatial field applications (10–20 m) and are not consistently available due to long flyover intervals and additional time gaps during critical growth stages due to cloudy conditions. Aircraft and UAVs are also influenced by weather conditions and operator issues (Putra & Soni, 2020) and are more expensive to employ. Although above-canopy spectral reflectance imaging in some cases may still be an effective and non-destructive chlorophyll sensing approach, it considers the upper canopy as a homogeneous horizontal plane (He et al., 2020; Winterhalter et al., 2012) and does not account for the substantial upward variation of N content in leaves.

The RGB spectrum is useful in capturing changes in the relative expression of pigments in plants. Chlorophylls principally absorb light in the Blue and Red range and therefore reflect prominently in the Green. Chlorophylls contain nitrogen and are not very stable compounds that need to be continuously synthesized. They are therefore most strongly associated with N availability in a leaf. Carotenoid pigments primarily absorb in the Blue-Green wavelength range and reflect primarily in the Green–Red (yellow). Carotenoids are more stable and persistent than chlorophylls and when the latter is lost from the leaf due to N stress, the yellow carotenoids become more prominent (Demetriades Shah & Court, 1987; Wu et al., 2019). Due to physiological preference for resource allocation to upper leaves in maize plants, chlorophyll deficiency and differential pigment expression is most prominently expressed in the lower canopy (Chen & Wang, 2022; Geng et al., 2022). I.e., N

deficient maize shows chlorophyll loss as a general progression of yellowing (chlorosis) and paling of older leaves from the bottom of the plant. A correlation therefore exists between the RGB reflectance spectra and leaf nitrogen status. The latter is difficult to assess from above because (i) early season canopy images are dominated by the soil background and plants typically do not exhibit stress yet, or (ii) in more developed canopies, the image is dominated by upper leaves and lower leaves are mostly hidden.

Image acquisition is the initial phase where the object of interest is captured through a digital camera and collected images are stored for further analysis and interpretation. Recent studies have successfully evaluated the N status of vegetation by using digital cameras for direct-leaf measurement (Anderson et al., 2016; Shannon et al., 2018; Shi et al., 2020). However, due to the complexity of field environments, including different crop growth stages, the identification of N status in maize remains challenging with currently available technologies through above-canopy-based sensing. To the best of our knowledge, there are no embedded camera systems available for farming vehicles that can transfer high-resolution video imagery from the under-canopy position directly for analysis. Collecting continuous imagery (video) from an under-canopy position during mid-growing season using RGB cameras on field robots may be a promising low-cost approach for N deficiency detection at high spatial resolution, especially when field passes for N stress detection and sidedress applications can be combined with other agronomic practices like cover crop interseeding and weed escape detection and control. Therefore, the primary objective of this study is to assess the effectiveness of a robot-mounted RGB imaging system in detecting within-field variability of N deficiency in maize through high-resolution under-canopy imaging. By analyzing spatial patterns of normalized difference (ND) color indices derived from RGB imagery captured at 30 frames/sec, we aim to determine the sensitivity of RGB-derived indices in identifying N stress at varying spatial scales and N application rates.

Materials and methods

This study was conducted under field conditions with four different N rate experiments where the $(R-B)/(R+B)$ normalized difference (ND) color index was used to assess field variability within and among N rate treatments. The study sites involved maize production and were located on a research farm in Minnesota (Rosemount, MN: 44.71N, 93.08W) in 2019, a research farm in New York (Aurora, NY: 42.72N, 76.65W) in 2020, and two commercial farms in New York (Geneseo, NY: 42.47N, 77.48W; Covington, NY: 42.51N, 78.06W) in 2022. Agronomic details on the experimental sites are summarized in Table 6 (Appendix).

The Minnesota site is characterized by a continental climate with cold, often frigid winters and hot, humid summers. Growing degree days (GDD) accumulation (base 10 °C) between the planting date (20 May 2019) and sampling date (18 July 2019) was 592 (Table 7, Appendix). The site's soil is mapped as Waukegan silt loam (Fine-silty over sandy or sandy-skeletal, mixed, superactive, mesic Typic Hapludolls). The nitrogen rate plots were 20 m wide and 90 m long. The New York research farm site is characterized by a humid continental climate, and accumulated 693 GDD between the 2020 planting date (22 May) and the sampling date (15, 22, and 29 July). The site is mapped as Kendaia-Lyons silt loam (Fine-loamy, mixed, semiactive, nonacid, mesic Aeric Endoaquepts; 38.8% of field area),

and Lima silt loam (Fine-loamy, mixed, semiactive, mesic Oxyaquic Hapludalf; 61.2% of field area), respectively (WSS, 2022).

The New York commercial farm sites (Geneseo, NY and Covington, NY) accumulated 637 GDD between the 2022 planting date (14 May) and the sampling date (25 July). The Geneseo field was mapped as Conesus silt loam (Fine-loamy, mixed, active, mesic Glossaquic Hapludalfs, 100% of field area), and the Covington field was mapped as Appleton gravelly silt loam (Fine-loamy, mixed, active, mesic Aeric Endoaqualfs; 48.8% of field area), Conesus gravelly silt loam (Fine-loamy, mixed, active, mesic Glossaquic Hapludalfs; 44.5% of field area), and Burdett silt loam (Fine-loamy, mixed, active, mesic Aeric Endoaqualfs; 6.7% of field area) (WSS, 2022).

The Minnesota trial included five N rates: 58, 100, 143, 225, and 271 N kg ha^{-1} (30% UAN), in spatially-balanced randomized complete block designs (van Es et al., 2007a, 2007b) with three replicates (Fig. 1). The nitrogen rate blocks were 8 rows (6 m wide). In the year prior to the study, the Minnesota site had been planted with wheat (*Triticum aestivum L.*). At the Aurora, NY site, two N rates were used: 90 and 145 kg ha^{-1} (30% UAN) in 2020, with a systematic design in four replicates (Fig. 1). The nitrogen rate plots were 24 rows (20 m) wide and 136 m length in 2020 and had been planted with maize in the years prior to the study (Table 6, Appendix). The highest N rate (145 kg^{-1}) was recommended by the Adapt-N software (Ever.Ag; Lewisville, Texas; Melkonian et al., 2008), and the lower rate (90 kg ha^{-1}) targeted mild nitrogen stress levels. The 2020 season was an unusually dry season during June and early July, a critical period for N gains and losses (Sogbedji et al., 2001), which presumably reduced the N stress from the lower rate. At the NY commercial

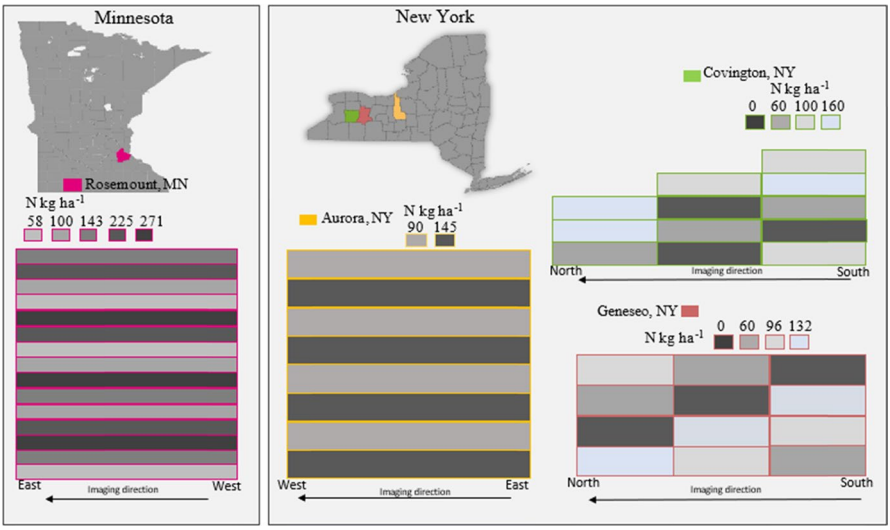

Fig. 1 Detailed layouts of N application trials conducted at four locations showing the experimental plots and the direction of imaging. In Minnesota, the site features horizontal bands indicating nitrogen application rates from 58 to 271 kg ha^{-1}, with imaging direction running from west to east. The New York sites include: Aurora, with bands illustrating two N application rates of 90 and 145 kg ha^{-1}, imaged from east to west; Covington, showing a grid layout with N rates ranging from 0 to 160 kg ha^{-1}, imaged from south to north; and Geneseo, where a similar grid layout presents N rates from 0 to 132 kg ha^{-1}, also imaged from south to north. The colored blocks represent different N application rates, and the arrows denote the direction of imaging across the experimental plots (Color figure online)

farms in 2022, four N rates were used (0, 60, 96, 132 N kg ha^{-1}; 30% UAN) at the Geneseo field laid out in a completely randomized design in three replicates, and four N rates were used (0, 60, 100, 160 N kg ha^{-1}; 30% UAN) at the Covington in a field spatially-balanced randomized complete block designs (van Es et al., 2007a, 2007b) (Fig. 1). The nitrogen rate plots were 48 rows (40 m) wide and 110 m long, and 12 rows (10 m) wide and 144 m long in the Geneseo and Covington fields, respectively. The sites had in the previous year been planted with forage small grains plus legume, and maize in the Geneseo and Covington fields, respectively. The Covington field had received pig (*Sus scrofa domesticus*) manure slurry (36,819.8 L ha^{-1}) during the previous fall.

The N rates were designed to reflect site-specific agronomic objectives and environmental conditions. In Minnesota (2019), the gradient (58–271 kg N ha^{-1}) tested ND's response across deficiency-to-excess extremes in high-fertility silt loam soils. At Aurora, NY (2020), Adapt-N recommendations (145 kg ha^{-1}) and suboptimal rates (90 kg ha^{-1}) assessed ND's sensitivity under mild stress in a drought-affected season. For NY commercial farms (2022), lower rates (0–160 kg ha^{-1}) accounted for residual N from legumes/fall manure, mimicking sustainable practices. This variability ensured the proposed method's sensitivity across heterogeneous soils, climates, and management systems, critical for scalable precision N management.

Mobile platform for RGB image collection

This section provides an overview of the methodologies and materials employed in the purpose-built construction of the mobile platform, a prototype ground robot. The platform was designed to operate under real field conditions, with adjustable mobility (speed, path control) to ensure standardized imaging and minimized errors. While the term"robot"may imply full autonomy, the prototype system is a human-guided platform optimized for precise, repeatable data acquisition. The processes involved in assembling the ground robot, integrating its control and sensing systems, and developing the software and applications required for its remote operation are outlined. The roles and functionalities of these components are shown in Table 8 (Appendix), providing an overview of the software and hardware used in the building process and their function.

Mobility design and assembly

The robotic mobility system was designed to effectively navigate through row-crop (maize) fields, prioritizing stability, maneuverability, and the ability to capture continuous imagery in the under-canopy environment. The robot's design was based on common maize field requirements and was created using computer-aided design (CAD) software (Autodesk Inventor Professional, 2022). Additionally, simulation of the robot's movements was performed using Blender (Blender, 2022). The robot has dimensions of 600 mm width, 670 mm length, and 320 mm height. The motors were chosen to ensure they provide the necessary propulsion for navigating field terrain. The mechanical structure and technical drawings of the robot are shown in Fig. 2. The locomotion was facilitated by four distinct motors, each powered by batteries with voltage regulators to ensure a consistent energy supply. Raspberry Pi was utilized for remote control and real-time video feed, which relayed visual

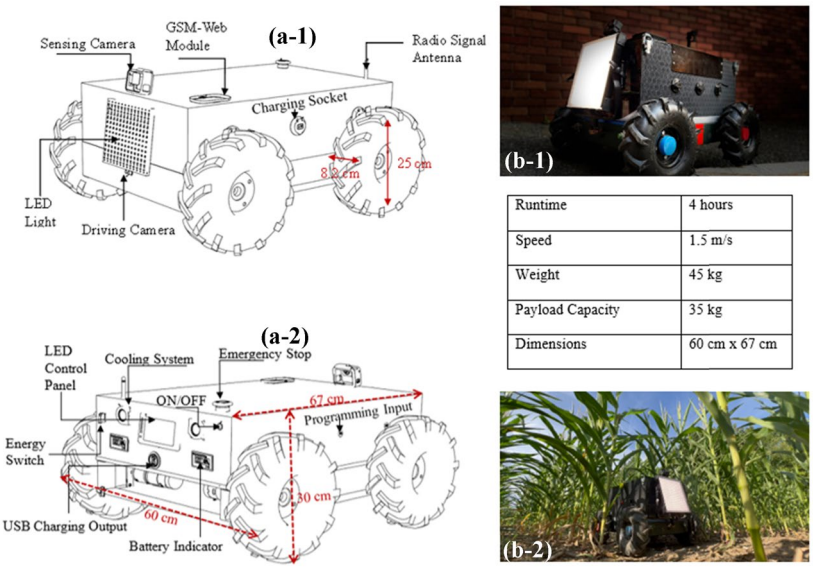

Runtime	4 hours
Speed	1.5 m/s
Weight	45 kg
Payload Capacity	35 kg
Dimensions	60 cm x 67 cm

Fig. 2 Purpose-built field robot technical drawings and photographs. **a-1**: Front view highlighting key components. **a-2**: Rear view highlighting key components. **b-1**: Assembled robot frontal view with sensing camera and LED lighting. **b-2** Field operation in maize. An accompanying video (Online Resource 1, named Robot.mp4) provides a dynamic illustration of the robot's operational capabilities to collect field imagery data

driving data through a custom-developed application. Unity's UI components were used to create an interface with joystick controls and other elements to control the robot.

Control system and sensing

Central to the robot's operation is a control system, comprising a RoboClaw motor controller (Basicmicro, 2023). An Arduino Mega 2560 Rev3 (Arduino, 2023) microcontroller board was used to program and test various motor control algorithms. The board was chosen for its flexibility and compatibility with the RoboClaw 2 × 30A motor controller, which made it easy to communicate with the controller and program custom motor control logic. This setup enabled precise control over the robot's movements, allowing for the execution of complex navigation algorithms necessary for operation in the field. A GoPro7 Black camera was mounted on the robot for high-resolution RGB video image processing. This approach ensured that detailed visual datasets could be collected efficiently during field navigation and analyzed post-mission to extract valuable insights.

High-resolution image collection and processing

Continuous imagery was acquired with a GoPro7 Black camera mounted on the robot, with images saved in video file (.MP4) format with 2704Wx2028H, 24-bit RGB color resolution, and video recorded at 30 frames per second (fps). The steps for the image processing for a maize N status detection algorithm under field conditions included (1) Collection of RGB

video imagery in daytime or nighttime, in both cases with LED lighting (previous studies showed benefits of supplemental LED lighting in daytime); (2) Extraction of the integral frames of recorded videos; (3) Applying filtering thresholds to remove undesirable backgrounds; (4) Extracting RGB color patterns from each pixel of a whole image, and saving the extracted color patterns as numerical Digital Number (DN) values for further statistical analysis; (5) Creating the metadata from extracted frames with GPS locations; (6) Final classification of created data for adjustable spatial resolution of desired management scale, and (7) Conducting statistical analyses. Steps 2, 3, and 4 were conducted using the purpose-built image processing software Leaf-N™, which was created for this study to analyze nitrogen stress through under-canopy RGB imagery.

RGB video image collection in daytime and nighttime

Light intensity changes during the day and the proposed N sensing algorithm aims to be applied under any light conditions. Continuous image collection was achieved at a consistent robot speed of 1.5 m/s and maize rows were recorded in progressive scans with supplemental LED light from a front-mounted panel (Dazzne D45 C, 14 inch Key Light with 5500 K 45W 19000 Lux CRI 96; Fig. 2).

Extracting video frames, image filtering, and RGB processing

From each video, the image frames were extracted in the order of recorded video as"integral frames", which means that each frame is being extracted for further processing. The total number of extracted frames depended on video length, and thereby the length of the scanned maize row. For example, if the N plot is 100-m length, the robot completes the data collection at 30 fps in 66.6 s, yielding a total of 1998 extracted images. After image extraction, thresholding was applied to the original images before RGB digital numbers (DNs) were obtained. The 30-degree upward angle of the camera position on the robotic ground vehicle required filtering of sky pixels, which was done by excluding RGB values greater than 150 (i.e., 151–255; Fig. 16, Appendix). Part of the images also included pixels representing soil which were filtered out by applying an HSV color model on extracted images to precisely remove soil pixels (Fig. 16c, Appendix). Thresholding limits can be arranged using the first extracted frame and applied to the rest of images automatically in the Leaf-N™, software, which overcomes the limitations of thresholding methods in standard commercial image processing algorithms.

Metadata from extracted frames with GPS locations

GoPro writes metadata in their proprietary open-source Go-Pro Metadata Format (GPMF) which is written as a track (video and audio) that runs in parallel so that the data matches up correctly. Video files have metadata for the complete video and for different times in the video (e.g., GPS values). These metadata hidden in each frame were extracted from the videos using the EXIF tool (ExifTool; Harvey, 2022).

Data classification at adjustable spatial resolution

In this context, the term frame classification refers to the process of precisely locating each extracted image within the scanned row in the field and accurately classifying it to obtain the desired resolution. As the vehicle speed was around 1.5 m/s, the RGB values of each row spanning a 6 m distance at 30 fps represent the ND values of 120 images. Frame classification is used in the process of calculating the degree of spatial overlap between successive video frames. It is used to sequence video frames by calculating spatial shifts in row directions from one frame to the next. This is highly time consuming and has limitations on accuracy, and we therefore developed a two-step image processing method. The first involves creating metadata with extracted GPS locations for each frame. The second adapts the embedded metadata information to the frames recorded between maize rows. Then classification was done within the extracted RGB pixel values (DN's) of each frame with their precise locations, regardless of the processing time needed.

Normalized difference color intensity (R-B/R + B) model

Normalized difference color intensity refers to the calculated value of the (R-B)/(R + B) index, which was found to be the most valuable RGB-derived index for lower-canopy maize N sensing. This study presents a fast process that is adaptable to different management scales. For this, data generated from the previous process were incorporated into new functions and algorithms that perform accurate image processing for the specific purpose of N sensing from an under-canopy perspective. Geo-referenced image data, with extracted features involving n frames in order of 1, 3, 5,..., n, were compiled in RGB color space and saved as 30 observations in every 1.5 m row distance sequence. The features of each frame were automatically saved in the same order as they appeared during frame creation in the form of image data. First, average RGB values were normalized for each image and the (R-B)/(R + B) index was derived to represent maize N stress. An average Normalized Difference (ND; R-B/R + B) of 30 images was assigned to every 1.5 m section of scanned maize row. Then, Eq. 1 was applied sequentially, resuming after every 30 images until the final extracted frame:

$$\mathrm{ND} = \frac{((R_{1.jpg} + R_{2.jpg} + R_{3.jpg+} \ldots\ldots\ldots + R_{30.jpg}) - ((B_{1.jpg} + B_{2.jpg} + B_{3.jpg} \ldots\ldots\ldots + B_{30jpg}))}{((R_{1.jpg} + R_{2.jpg} + R_{3.jpg+} \ldots\ldots\ldots + R_{30.jpg}) + ((B_{1.jpg} + B_{2.jpg} + B_{3.jpg} \ldots\ldots\ldots + B_{30.jpg}))} \quad (1)$$

where ND represents the average ND value calculated for a 1.5-m scanned distance along the row.

The steps of this process can be broken down as follows: (1) Extracting: The extracted images are divided into groups of 30, (2) Normalization: For each group of 30 images, the average normalized color intensity is calculated, (3) Spatial Assignment: The calculated average intensity of each group is assigned to every 1.5 m of scanned row, and (4) Sequential Application: The process repeats from step 2 for the next group of 30 images until the final frame is extracted. These ND values were calculated for every 120 images as an average Normalized Difference (ND; R-B/R + B) value. Finally, these ND values were assigned to every 6 m section of the scanned maize row.

Interactive RGB video data visualization

The raw RGB video data was first used to extract individual frames before thresholding. For each frame, the average RGB values were calculated to obtain a quantitative measure of the color properties of the maize leaves. These RGB values were then used to create a color-coded map that visualizes the spatial distribution of color properties across the field. The geo-location of the robot platform and the speed of the robot were used to align the frames and reconstruct the field of view in a spatially accurate way. The location of the robot in the field, as well as the direction of sampling, were also recorded to allow for precise spatial referencing of the data. An interactive video interface was developed (Fig. 3) that includes the original RGB video (top left), the filtered RGB video (main image), the average RGB values of each frame and ND values for each set of 30 frames (top center), as well as the geo-location, speed of the robot, sampling direction, distance in row, and other metadata associated with each frame. This allows for the exploration of the spatial and temporal variation of color properties of the under-canopy maize rows in a more engaging and informative way in real-time. The color-coded map, along with the metadata associated with each frame, provides a valuable tool for site-specific N management.

Statistical analysis

The (R-B)/(R+B)-based ND index (representing normalized difference color intensity) from the image data was analyzed using the R statistical language (version 4.2.2; R Core Team, 2022) packages ggthemes (version 4.2.4; Arnold, 2021), effectsize (version 0.8.2; Ben-Shachar et al., 2022), datawizard (version 0.6.4; Patil et al., 2022), and ggplot2 (version 3.4.0; Wickham, 2016). Analysis of variance (ANOVA) was used to analyze significant

Fig. 3 Visualization of maize canopy analysis through RGB video data processing. This interface showcases the integration of processed RGB video data with spatial metadata for enhanced under-canopy crop monitoring, including (1) the original and filtered RGB video frames, highlighted with a white box; (2) color-coded mapping based on average RGB and ND values for sets of frames; and (3) essential metadata such as geolocation, robot speed, and sampling direction

differences among applied N rates. Prior to conducting ANOVA, assumptions of normality, homogeneity of variance, and independence of residuals were assessed and met. Three linear model regressions were employed to determine the strength of the relationships between the N rates and ND in the Minnesota and New York multi-N rate experiments. lm1: based on plot treatment means only; lm2: accounting for block effects (removing larger-scale field spatial variability), and lm3: based on individual image observations. The coefficient of determination (R^2) was used to compare the performance of the (R-B)/(R+B)-based ND index. Tukey's Honest Significant Difference (HSD) test was conducted at a significance level of $\alpha = 0.05$ for mean comparisons.

Geostatistical analysis (Yates & Warrick, 2002), including the calculation of sample variograms, was performed using ArcGIS Pro Geostatistical Wizard 3.0.1 (Esri, 2021) to assess the structure of local dependence, as characterized by fitted semivariograms models. The aim of the semivariograms analysis was to characterize the local spatial structure of ND index values in a field, rather than to predict values at unsampled locations. The spatial structure of the leaf color response was separately evaluated for each N rate because spatial variances and autocorrelations were expected to be nonhomogeneous among N rates. The semivariograms were developed based on a lag distance of 0.5 m and a total of 90 lags. Setting the lag distance to 0.5 m allowed for the capture of spatial variability within each N rate treatment plot and identify distinct spatial structures or patterns at that scale. The non-trend spherical model was applied to the semivariograms, defined as a piecewise function (Eq. 2):

$$\gamma(h) = \begin{cases} C_0 + C_1 \left[1.5\left(\frac{h}{a}\right) - 0.5\left(\frac{h}{a}\right)^3\right], & \text{for } 0 \le h \le a \\ C_0 + C_{1,} & \text{for } 0 \le h \le a \end{cases} \quad (2)$$

where h is the separation distance, a is the range, C_0 is the nugget (effect), and C_1 is the sill variance component (Yates & Warrick, 2002). These parameters were derived to characterize the spatial structure of variability in the (R−B)/(R+B)-based ND index values for different N rates. Although alternative models (e.g., exponential, Gaussian, linear) were considered and tested, the spherical model was adopted across treatments to maintain consistency in parameter interpretation. The spherical model was also found to provide reliable fits across most treatments based on visual and residual diagnostics.

N stress mapping

Maps were developed using the ArcGIS Pro software (Esri, 2021) to visualize the spatial distribution of the (R-B)/(R+B)-based ND index values. A resolution of 6-m was chosen based on the semivariogram analysis, which identified the appropriate sampling size necessary to accurately capture the spatial variability of the scanned row. Additionally, previous power analysis results (Bestas et al., 2025) were used when determining the resolution, as they provided additional guidance on the ideal sampling size. In addition to traditional 2D mapping, metadata extraction capabilities were utilized to generate 3D mapping of the field, facilitating detailed field inspection (see"mapped.mp4"in Online Resource 2).

Results and discussion

Across four field trials in Minnesota and New York, each with distinct environmental and management conditions, the R and B-based ND index values consistently decreased as applied N rates increased under both daytime and nighttime imaging conditions. The lowest N treatments were associated with the highest ND values, reflecting more pronounced chlorophyll depletion in the lower canopy. Nighttime imaging produced more stable ND measurements and stronger correlations with N rates, likely due to reduced ambient light interference. These findings demonstrate that under-canopy RGB imaging is capable of capturing meaningful spatial and temporal variation in leaf pigment expression and crop N status, influenced by both N availability and environmental variability.

This observed spectral response aligns with prior studies that used visible bands to estimate plant nitrogen status and chlorophyll levels (Dutta et al., 2015; Pagola et al., 2009; Yadav et al., 2010; Yue et al., 2021). Virtanen et al. (2022) reported that yellowing leaves show increased reflectance in the red band with less change in the blue band, supporting the ND formulation used here. It also implies that visual differences in leaf "greenness" are actually less expressed in the G band itself. Additional studies (Brodersen & Vogelmann, 2010; Liu et al., 2021; Xiao et al., 2016; Zhang et al., 2020) support the differential role of R and B bands in detecting N-related pigment changes. Dong et al. (2020) also highlighted how growth stage influences N response, consistent with the decreasing ND differences observed between early and late sampling dates (DAP54 to DAP66). Our findings agree with those of Bajwa et al. (1999) and Xu et al. (2021), reinforcing the ND trend across growth stages and N rates.

ND and N rates in multi-rate Minnesota trial

Table 1 shows descriptive statistics of the ND (R-B/R+B) index by N rate (58, 100, 143, 225, 271 kg N ha^{-1}) for the Minnesota trial. Tukey's HSD test showed that the ND index differed significantly by N rate ($p<0.05$), and the ND index gradually decreased with increased N rate (from 0.247 for 58 kg ha^{-1} to 0.178 for 271 kg ha^{-1}; $R^2=0.82$). Based on an ANOVA model, the main effect of N is statistically significant ($p=0.016$; Eta2 (partial)=0.75, 95% CI [0.23,1.00]). Table 2 shows the relationship between ND values and applied N rates through three linear mixed model analyses: lm1 (based on plot treatment means only), lm2 (accounting for block effects and removing larger-scale field spatial variability), and lm3 (based on individual image observations). The marginal R^2 considers only the variance of the fixed effects (without the random effects), while the conditional R^2 takes both the fixed and random effects into account. For 6-m resolutions, the findings are as follows; for the

Table 1 Descriptive statistics (mean(sd)) of (R-B)/(R+B) based ND index and N rates (58, 100, 143, 225, 271 N kg ha^{-1}) in Minnesota using Tukey HSD

Field	GS†	N rates kg ha^{-1}	ND (R-B/R+B) mean (sd)‡
MN	V16	58	0.247(0.05)a
		100	0.227(0.04)ab
		143	0.209(0.04)b
		225	0.213(0.03)b
		271	0.178(0.02)c

†GS: Growth Stage. ‡Based on model<-ANOVA (mean~block+treatment, data=means), α=0.05

Table 2 Linear mixed model for ND by N rates and block effect in Minnesota

Model	(R-B)/R-B) based ND	
	6-m	
	P	R^2
lm1	< 0.001	0.47
lm2	< 0.001	0.82
lm3	< 0.001	0.47
Observations	23,280	

lm1 <—lm(RGBmean ~ treatment, data = plot_means); lm2 <—lm(RGBmean ~ block + treatment, data = plot_means); lm3 <—lm(ND ~ treatment, data = individual_images)

A total of 23,280 frames were extracted from videos (~ 1,560 frames × 15 plots), and ND values were calculated by averaging every 120 frames, resulting in 13 ND observations per plot (6 m resolution). This yielded a total of 195 ND values (13 × 15). For lm1 and lm2, the 13 ND values per plot were further averaged to obtain one RGB mean per treatment-block combination. Thus, both lm1 and lm2 were based on 15 observations (5 N rates × 3 blocks), enabling valid estimation of treatment and block effects. RGB mean represents the averaged ND value per treatment-block combination. For lm3, the model used all 195 individual image-based ND values without aggregation to capture within-plot variability

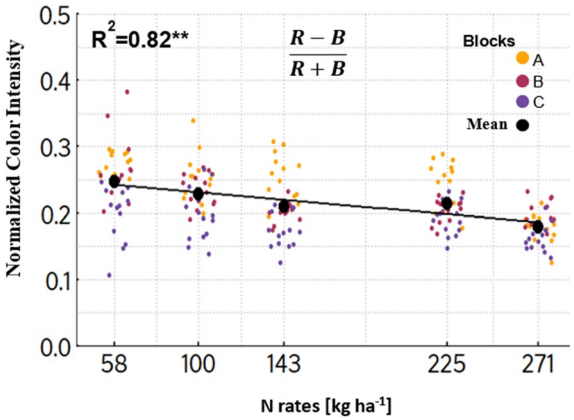

Fig. 4 Relationship between the (R–B)/(R + B)-based ND index and applied nitrogen rates (58, 100, 143, 225, and 271 kg N ha^{-1}) in the Minnesota 2019 trial. Each point represents a 6-m ND observation, color-coded by block. Black circles represent treatment-level means averaged across three blocks (n ≈ 39 ND values per rate), 58 kg N ha^{-1} = 0.247 ± 0.050; 100 kg N ha^{-1} = 0.227 ± 0.040; 143 kg N ha^{-1} = 0.209 ± 0.040; 225 kg N ha^{-1} = 0.213 ± 0.030; 271 kg N ha^{-1} = 0.178 ± 0.020. The fitted regression line is based on the lm2 model (ND ~ block + treatment) using plot-level means. The regression line and coefficient of determination (R^2 = 0.82) are based on the lm2 model

linear model lm2 (accounting for significant block effects, based on mean values), the total explanatory power was high (conditional R^2 = 0.82) while the component related to the fixed effects alone was lower (marginal R^2 = 0.32) (Fig. 4).

ND index and applied N rates in two-rate trial, Aurora, NY-2020

The ND (R-B)/(R + B) index with N rates 90 and 145 kg N ha^{-1} (Adapt-N-based and Adapt-N minus 55 kg N ha^{-1}) for multiple dates showed that the index varied significantly by N rate ($p < 0.05$); the ND index had the highest mean value in the lower N rates (0.285, 0.111,

Table 3 Descriptive statistics (mean(sd)) of ND index

Field	GS†	N rate kg ha^{-1}	$\frac{R-B}{R+B}$ ‡
Aurora, NY 2020	DAP54	90	0.285(0.01)a
		145	0.243(0.01)b
	DAP60	90	0.111(0.01)a
		145	0.07(0.01)b
	DAP66	90	0.115(0.01)a
		145	0.10(0.01)b

(0, 145 kg N ha^{-1}) and growth stages (DAP54, DAP60, DAP66 in Aurora, NY 2020. ‡Based on model<-ANOVA (mean~block+treatment, data=means), $\alpha=0.05$. Each of the 8 plots (2 N rates×4 blocks) in the Aurora, NY 2020 trial was 136 m long and recorded at 30 FPS, yielding~2,720 frames per plot per sampling date. ND values were calculated every 120 frames (6 m), resulting in~23 values per plot per date and~552 total values across three dates (DAP54, DAP60, DAP66). One aggregated ND value per plot was used in each ANOVA (n=8)

†DAP: Day after planting

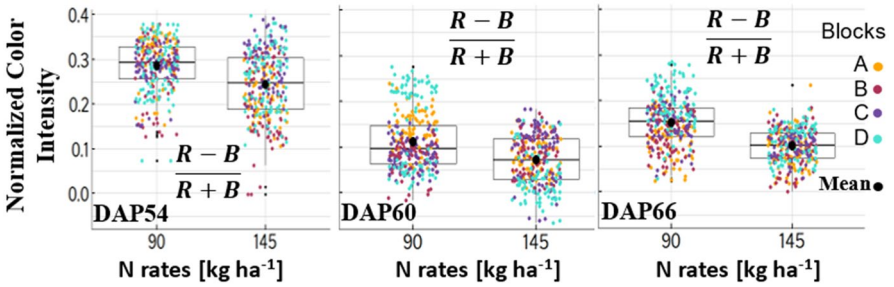

Fig. 5 (R-B)/(R+B)-based ND index values for nitrogen rates (0, 145 kg N ha^{-1}) and growth stages (DAP54, DAP60, DAP66) in Aurora, NY 2020. Each point represents a 6-m ND observation color-coded by block. Black circles represent treatment-level means averaged across four blocks (n ≈ 92 ND values per N rate per date) (Color figure online)

0.115 for 90 kg N ha^{-1} and 0.243, 0.07, 0.10 for 145 kg N ha^{-1} at DAP=54, DAP=60, DAP=66, respectively) and decreased with N rate (Table 3; Fig. 5). An ANOVA was conducted to compare the effect of N rates on the ND index. There was a significant effect of N rates on ND values ($p<0.001$). Mean (R-B)/(R+B)-based ND index values for the lower N rate were significantly different than the higher N rate. Specifically, results suggest that maize leaves express higher color intensity in B and R bands when they experience lower levels of N.

ND index and applied N rates in multi-rate on-farm trials

For the Covington, NY 2022 trial, the ND index varied significantly by N rate ($p<0.05$). (R-B)/(R+B) had the highest mean value in the lowest N rates (0.221 for 0 ha^{-1}; Table 4; Fig. 6) and decreased with increasing N rate. Based on the ANOVA results, the main effect of N supply on color intensity value (ND) was statistically significant while the main effect of block was not significant. An analysis of variance based on linear regression indicated a statistically significant effect on ND of N rates ($p<0.001$). The model included Block as

Table 4 Linear models for ND by N rates and block effect in Covington NY-2022

(R-B)/R-B) based ND		
Model	p	R^2
lm1	< 0.001	0.781
lm2	< 0.001	0.772
lm3	< 0.001	0.201

Each of the 12 experimental plots in Covington, NY 2022 (4 N rates × 3 blocks) was 144 m long and recorded at 30 fps, producing approximately 2,880 frames per plot. ND values were computed every 120 frames (6-m resolution), resulting in ~ 24 ND observations per plot and ~ 288 total ND values across the trial

lm1 <—lm(RGBmean ~ treatment, data = plot_means); lm2 <—lm(RGBmean ~ block + treatment, data = plot_means); lm3 <—lm(ND ~ treatment, data = individual_images). For lm1 and lm2, the ~ 24 ND values per plot were averaged to obtain one RGBmean per treatment × block combination. RGBmean represents the averaged ND value per treatment-block combination. Thus, both lm1 and lm2 were based on 12 observations (4 N rates × 3 blocks). The lm3 model used all ~ 288 unaggregated ND values to assess within-plot variability

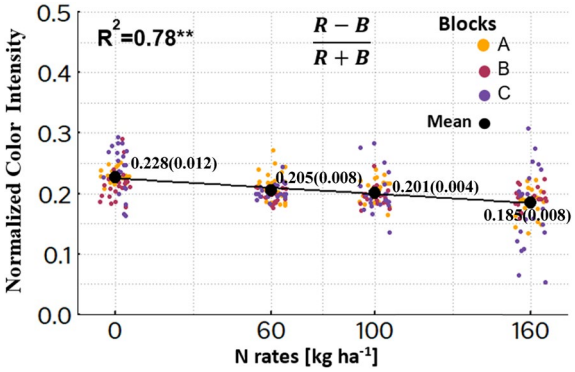

Fig. 6 Relationship between the (R–B)/(R + B)-based ND index and applied nitrogen rates (0, 60, 100, and 160 kg N ha^{-1}) in the Covington, NY 2022 trial. Each point represents a 6-m ND observation colored by block. Black circles represent treatment-level means averaged across three blocks (n = 72 ND values per rate), 0 kg N ha^{-1} = 0.228 ± 0.012; 60 kg N ha^{-1} = 0.205 ± 0.008; 100 kg N ha^{-1} = 0.201 ± 0.040; 160 kg N ha^{-1} = 0.185 ± 0.008. The fitted regression line is based on the lm2 model (ND ~ block + treatment) using plot-level means. The regression line and coefficient of determination (R^2 = 0.78) are based on the lm2 model

a random effect (formula: 1| block). A simple linear regression (based on plot treatment means only; Fig. 6 was conducted to predict the under-canopy ND color based on applied N rates (formula: mean values of ND (120 images) ~ N rates). The model explains a statistically significant and substantial proportion of variance (R^2 = 0.78, p = 0.002). The model's intercept, corresponding to a nitrogen rate of 0, was estimated to be 0.23 (95% CI [0.22, 0.23], p < 0.001).

The Covington trial exhibited nearly identical values for conditional (0.772) and marginal R^2 (0.781). This suggests that block-level variability contributed little to the explained variance at Covington, with most of the variation in ND values explained by fixed N rate effects. This difference likely reflects lower spatial heterogeneity in the Minnesota vs. Covington field, including higher organic matter content (2.8%) and fine-silty soil variability, combined with a wetter growing season (652.9 mm rainfall). In contrast, Covington had

lower organic matter content (1.2%), received uniform manure applications, and experienced drier conditions (321.8 mm rainfall), leading to more homogeneous field conditions.

For the Geneseo 2022 trial, image collection was performed during both nighttime and daytime, and a linear regression was conducted to predict under-canopy ND index based on applied N rates for both measurement conditions (Table 5). The lm2 model (accounting for Block effects) was statistically significant and explained a substantial proportion of variance ($R^2 = 0.80$, $p = 0.043$), indicating a good fit to the data. The effect of N treatment was also statistically significant and negative (95% CI [−2.79e-04, −9.91e-05], $p = 0.001$), which suggests that increasing N rates result in a decrease in under-canopy ND index values. The signal of ND index responses to applied N rates at nighttime with 5500 K LED lighting was found to be similar to that of daytime, but image-to-image noise (variability) was dramatically decreased for nighttime imaging (Table 5). The linear model's total explanatory power was moderate ($R^2 = 0.30$) in daytime measurements, but more substantial ($R^2 = 0.67$) in nighttime measurements (Table 5). Nighttime imaging therefore not only reduces image-to-image variability but also shows a stronger relationship between under-canopy ND index and applied N rates, indicating its potential to improve accuracy in predicting crop N status (Fig. 9a, b). The lm2 linear model explains a statistically significant and substantial proportion of variance ($R^2 = 0.92$, $p < 0.001$; Table 5). These findings suggest that nighttime imaging is more powerful for assessing under-canopy ND index response to N rates. The Covington, NY trial daytime resulted in slightly lower R^2 values than the Geneseo, NY trial daytime for the linear models, presumably due to manure applications in two previous falls (40,834.9 L/ha in 2020, and 96,303.4 L/ha, 13,002.4 L/ha, and 91,152.1 L/ha in 2021).

Figure 7 summarizes the ND index means for applied N rates in daytime and nighttime measurements at the Geneseo site, and shows the (R-B)/(R + B) index distribution based on image-averaged units of 6 m. It indicates differences both among and within treatment plots. Strong relationships existed for the ND index (R-B/R + B) under both daytime and nighttime imaging. Daytime and nighttime ND values generally decreased in parallel with increased N rates, and similar color responses were observed for both illumination conditions. In the

Table 5 Linear models for ND by N rates and Block effect, for both daytime and nighttime measurements conducted in Geneseo, NY in 2022

Model	(R-B/R + B) based ND			
	Daytime		Nighttime	
	p	R^2	*p*	R^2
lm1	< 0.001	0.54	< 0.001	0.80
lm2	< 0.001	0.80	< 0.001	0.92
lm3	< 0.001	0.30	< 0.001	0.67

Each of the 12 experimental plots (4 N rates × 3 replicates) was 110 m long and recorded at 30 fps, producing approximately 2,200 frames per plot per lighting condition. This resulted in 26,400 frames for daytime and 26,400 frames for nighttime, totaling 52,800 frames across the trial. ND values were computed every 120 frames (6-m resolution), resulting in approximately 18 ND observations per plot and 216 total ND values per lighting condition

lm1 <—lm(RGBmean ~ treatment, data = plot_means); lm2 <—lm(RGBmean ~ block + treatment, data = plot_means); lm3 <-lm(ND ~ treatment, data = individual_images). For lm1 and lm2, the 18 ND values per plot were averaged to obtain one RGBmean per treatment × replicate combination. RGBmean represents the averaged ND value per treatment-block combination. Thus, both lm1 and lm2 were based on 12 observations (4 N rates × 3 replicates) per condition. The lm3 model used all 216 unaggregated ND values per condition to assess within-plot variability, with 432 total ND values analyzed across both lighting conditions

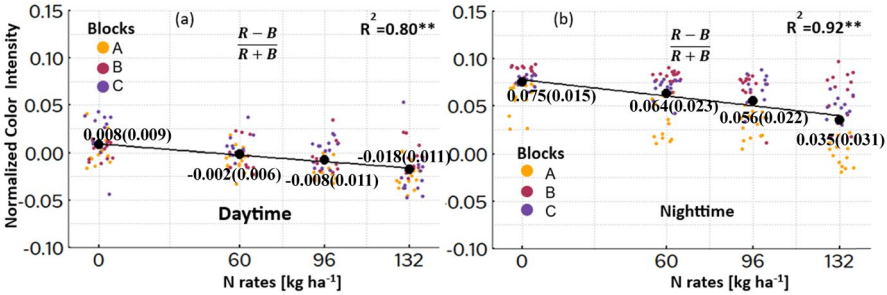

Fig. 7 Relationship between the (R–B)/(R+B)-based ND index and applied nitrogen rates (0, 60, 96, and 132 kg N ha^{-1}) in the Geneseo, NY 2022 trial under **a** daytime and **b** nighttime conditions. Each point represents a 6-m ND observation, color-coded by block. Black circles represent treatment-level means averaged across three blocks (n ≈ 54 ND values per rate). **a** Daytime: 0 kg N ha^{-1} = 0.008 ± 0.009; 60 kg N ha^{-1} = –0.002 ± 0.006; 96 kg N ha^{-1} = –0.008 ± 0.011; 132 kg N ha^{-1} = –0.018 ± 0.011. **b** Nighttime: 0 kg N ha^{-1} = 0.075 ± 0.015; 60 kg N ha^{-1} = 0.064 ± 0.023; 96 kg N ha^{-1} = 0.056 ± 0.022; 132 kg N ha^{-1} = 0.039 ± 0.031. The regression lines and coefficients of determination (R^2 = 0.80 for daytime, R^2 = 0.92 for nighttime) are based on the lm2 model (ND ~ block + treatment) using 12 plot-level means per lighting condition (Color figure online)

Geneseo trial, the ND index was consistently responsive to applied N rates in both daytime and nighttime measurements, indicating that it is a reliable indicator under different lighting conditions. However, the variability in image-to-image measurements was significantly lower in nighttime measurements, which may be due to the more controlled light environment (LED lights) in nighttime measurements. Given that chlorophyll in stems and leaves absorbs red incident light for photosynthesis, it is likely that the red wavelengths within the canopy at night were less scattered or transmitted (Sakamoto et al., 2010). Another possible explanation is that, while the measured color response intensities (ND) from under-canopy were derived from the direct LED lighting in nighttime, they were affected by scattered light and transmitted light from sunlight when sensed during the daytime. The near-zero ND values in daytime measurements likely result from ambient light variability rather than the absence of N status response. Nighttime conditions minimized this effect, enhancing ND detection across N rates.

Spatial distribution of ND index response to applied N rates

Understanding the spatial characteristics of under-canopy color properties is important for determining an appropriate spatial resolution for the image processing model in site-specific N applications, specifically in addressing treatment-induced spatial non-heterogeneity. Variogram analysis was performed to (i) quantify the spatial structure of variability, (ii) assess the spatial range for optimum N rate management, and (iii) determine whether spatial structures varied for different N rates, i.e., treatment-induced spatial non-heterogeneity (van Es,). Five semivariograms and a map were developed for N response considering each applied N rate (58, 100, 143, 225, 271 N kg ha^{-1}). Within each site unit (90-m length, 20-m width for applied nitrogen treatments), the ND values (mean (R-B/R+B)) were calculated for each N treatment.

Figure 8 shows semivariograms and associated model parameters for each N rate in the Minnesota 2019 trial. The spherical semivariograms model was characterized by its nug-

get (i.e., variability at distances smaller than the shortest distance between sample points including measurement error), sill (i.e., uncorrelated observed variation of the variable), and range (distance within which observations are spatially correlated). The range was 6.3 m for the lowest applied N rate plot of 58 N kg ha^{-1}, which is equivalent to the travel distance of the robotic vehicle in four seconds. The spherical model fitted to the ND data had a nugget (C0) of 0.00, and a partial sill (C) of 0.00206. For the applied N rate plot of 100 N kg ha^{-1}, the range was slightly lower at 5.6 m. Both the range and partial sills of the semivariograms gradually decreased with increasing N rates, down to 3.2 m and 0.0011, respectively for the highest N rate (271 N kg ha^{-1}; Fig. 9). This indicates that field variability tends to become less pronounced when N stress levels are reduced, i.e., the underlying variability in N availability is evened out and less defined by the inherent soil N supply (Mamo et al., 2003).

There was also an additional field trend in most cases, and an apparent "hole effect" that suggests repetitive field patterns and was most pronounced with the lowest N rate. Apparently under conditions of N deficiency recurring spatial patterns of variability emerge, likely due to patchy N availability or differential plant uptake efficiency. As N availability increases with higher N rates, these oscillatory patterns become less pronounced, suggesting that higher N applications create more uniform canopy response.

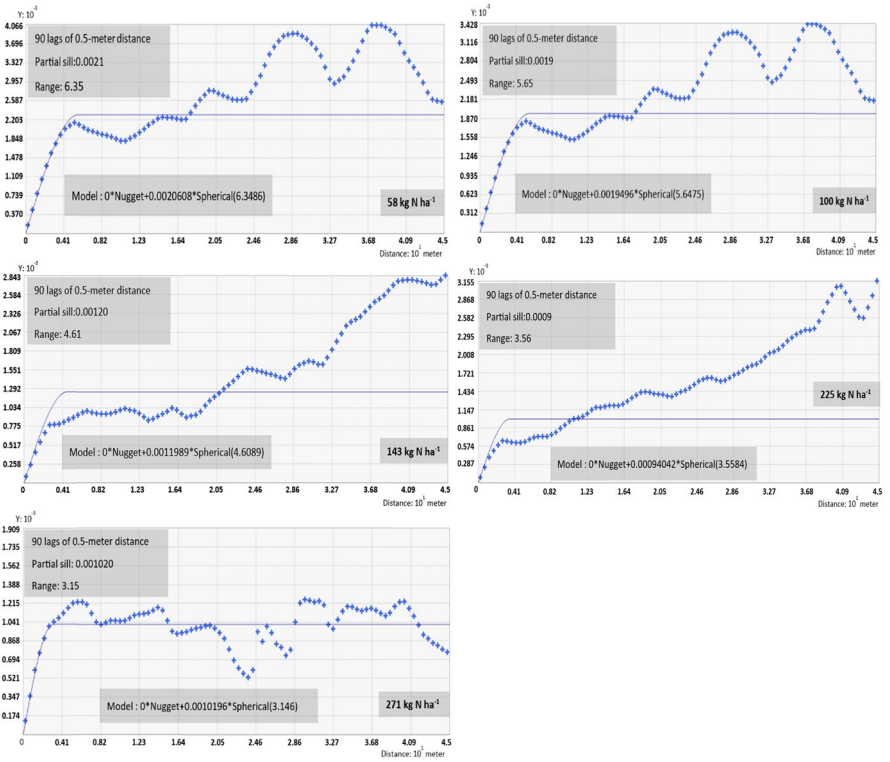

Fig. 8 Semivariograms of the (R-B)/(R+B)-based ND index for applied N rates (58, 100, 143, 225, and 271 kg N ha^{-1}) in the Minnesota 2019 trial. The x-axis represents distance in meters. Exceedances above the sill reflect structured trends and periodicity (hole effect). Detrending was tested but not applied, as it removed meaningful spatial trends relevant to field-scale N variability

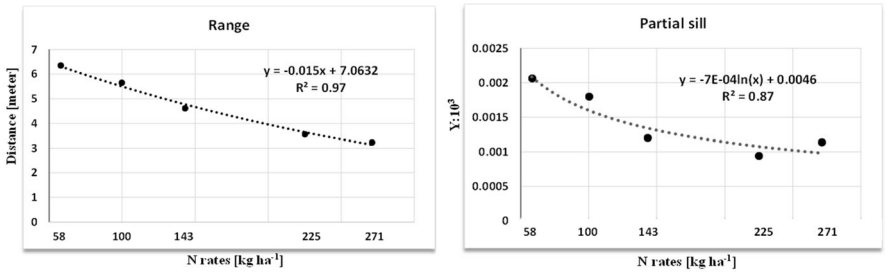

Fig. 9 Model parameters of the (R-B/R + N)-based ND index by applied N rates 58, 100, 143, 225, 271 N kg ha^{-1}) in Minnesota-2019

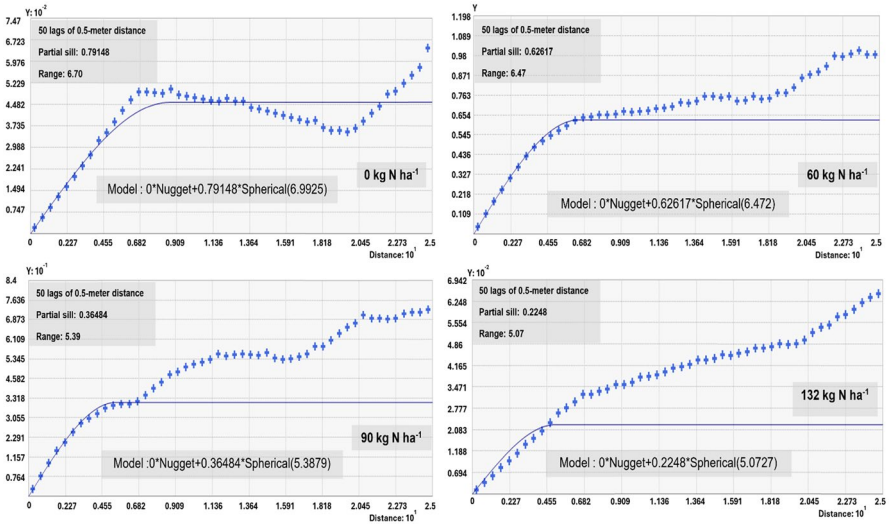

Fig. 10 Semivariograms of the (R-B)/(R + B)-based ND index for applied N rates (0, 60, 90, and 132 kg N ha^{-1}) in the Geneseo 2022 trial. The x-axis represents distance in meters. Exceedances above the sill reflect structured trends and periodicity (hole effect), rather than model error. Detrending was tested but not applied, as it removed meaningful spatial trends relevant to field-scale N variability

A similar trend emerged with the Geneseo, NY 2022 trial (Figs. 10 and 11), where ND index semivariograms were evaluated for four N rates (0, 60, 90, and 132 kg N ha^{-1}). Again, the fitted spherical models show a systematic decrease in both the range (from approximately 6.7 m down to 5.1 m) and partial sill (from about 0.79 down to 0.22) as N application rates increase. Overall, the spatial range was about 3.5–6 m, which suggests for this field that precision N application should involve adjustment of nitrogen rates at up to 6-m resolution. For the robotic imaging setup of this study, this would involve ND-based adjustments every 3–4 s (~100 images). GPS-guided variable-rate application systems can be calibrated for 6-m resolution, making implementation practically feasible in commercial farming. Also, the hole effect findings highlight spatial periodicity and potential benefits of site-specific management to enhance nitrogen use efficiency.

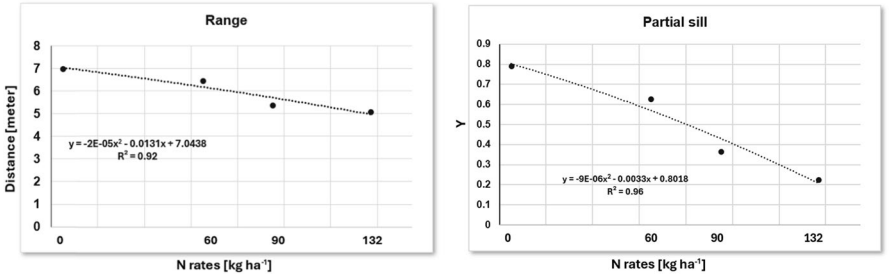

Fig. 11 Model parameters of the (R-B/R + N)-based ND index by applied N rates 0, 60, 90, 100 N kg ha^{-1}) in the 2022 Geneseo (NY)

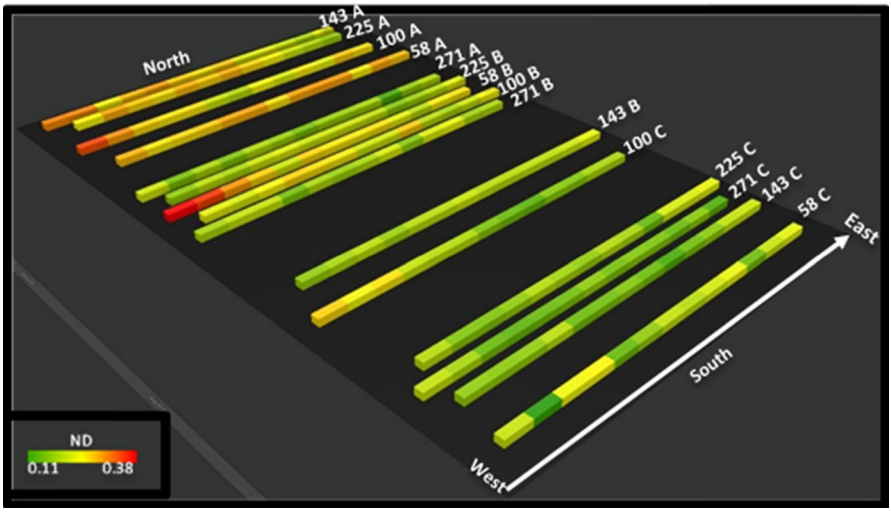

Fig. 12 The relationships between (R-B/R + B)-based ND index of maize under canopy leaf surface and applied N rates (58, 100, 143, 225, 271 kg ha^{-1}) in the Minnesota 2019 trial based on 6.0-m averaged values

Mapping nitrogen stress distribution

The analysis of the semivariograms provided valuable insights into the spatial structure of the ND index in response to different N rates in the maize field. This section focuses on visualizing the distribution of N stress in the field trials.

Minnesota trial

Figure 12 displays the color-coded ND index maps for each of the five N rates applied to the plot. The ND index values generally decreased with increasing N rate. The highest ND index values were observed in the 58 kg N kg ha^{-1} treatment plot (block 58A), with mean values ranging from 0.25 to 0.35 across the plot. Conversely, the lowest ND index values were observed in the 271 kg ha^{-1} treatment, with mean values ranging from 0.11 to 0.19

across the plot, similar to Ahmad and Reid (1996). However, although the overall relationship between ND value and N rate is strong (Fig. 12), this map indicates that the pigment-induced color expression varies considerably both by block (more apparent N stress on the southern end of the field) and along crop rows (E-W direction). This suggests the existence of considerable residual field-scale N stress variability that can potentially be managed using sensing and site-specific applications.

Aurora, NY-2020

The spatial distribution of ND index values based on 6-m distances along the row (Fig. 13) for the Aurora NY 2020 trial indicates that the lower N rate of 90 kg N ha^{-1} was generally associated with higher (more red) ND values than the 145 kg N ha^{-1} rate, which is consistent with previous studies. Like with the MN trial, considerable block and in-row variation existed, suggesting the presence of field patterns that were detected by the lower-canopy imaging. Although patterns were generally consistent and commensurate with N rates, the ND values varied by imaging date. DAP54 was measured at the end of a relatively dry period (total rainfall: 47.6 mm, Table 7), likely exacerbating nitrogen stress and resulting in elevated ND values, particularly in Block D. Conversely, DAP60 followed substantial rainfall events totaling 105.91 mm (Table 7), which likely facilitated nitrogen redistribution and uptake, leading to temporarily reduced ND values in Block D. By DAP66, cumulative rainfall had reached 202.58 mm (Table 7), stabilizing soil moisture conditions, with ND values in Block D becoming similar to those observed at DAP54. According to Plett et al. (2020), water availability in the soil is a factor that regulates the availability of nitrogen. For both DAP 60 and 66 measurements, the plots that received 90 kg N in Block D still exhibited the highest ND values, particularly in the half of the plot from the west side. Conversely, the plot that received 90 kg ha^{-1} N rate (suboptimal) in Block A showed gradually decreasing ND values for DAP 54, 60, and 66, presumably as more soil N became available from rainfall after the drought period. These findings highlight the importance of considering both nitrogen rate and spatial variability when making management decisions for optimizing nitrogen application in the field. Also, it suggests that timing of sensing (esp. relative to rainfall events) affects ND response and reduces the universality of the RGB sensing approach. Sensing efforts may require an additional information source, e.g., a dynamic simulation model output (Sela et al., 2016), to establish target fertilizer rates that may be modulated by RGB sensing output.

Covington NY-2022

Figure 14 shows the spatial distribution of the ND index (R-B)/(R+B) value in relation to the nitrogen rates (0, 60, 96, 132, N kg ha^{-1}) applied in the Covington NY-2022 field. The map highlights that the 60 kg ha^{-1} plot on the southeastern end of the field exhibited the highest ND values (greater than the nearby 0 kg ha^{-1} plot), whereas the adjacent plot with 160 kg N ha^{-1} plot had the lowest values. Additionally, the southern ends of both plots had the highest ND index values, while the middle of both plots showed a different pattern. The

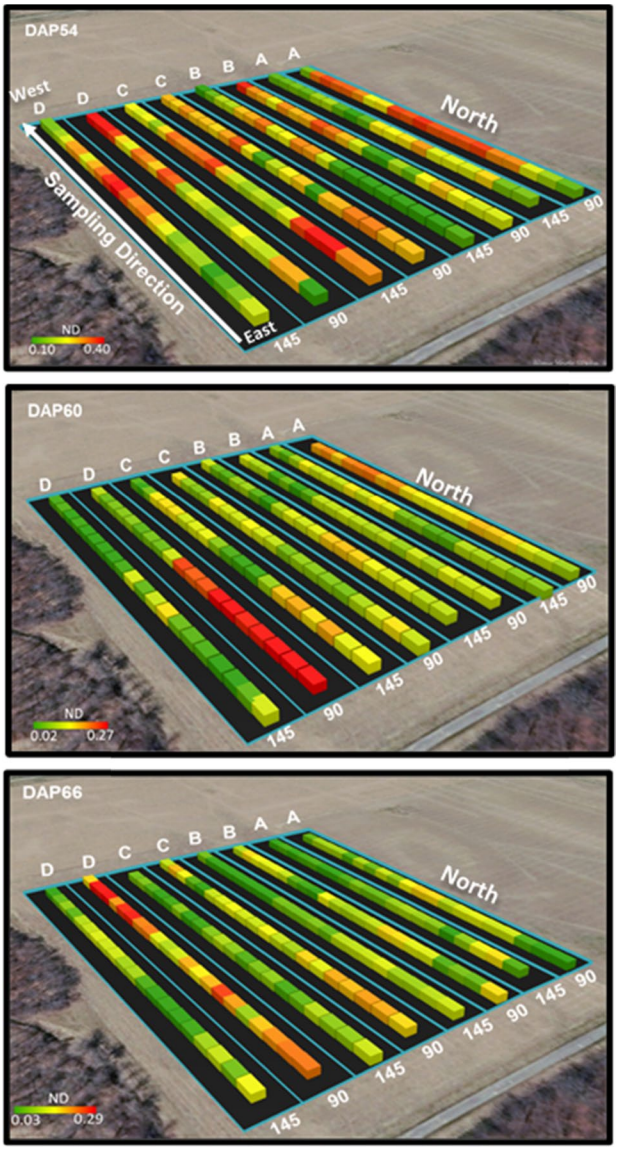

Fig. 13 Spatial distribution of (R-B)/(R+B)-based ND index according to the response of nitrogen rates (90, 145 kg N ha^{-1}) at DAP54, DAP60, DAP66 in Aurora, NY 2020. Based on average units along the crop row of 6.0 m

plots that received 0 kg N ha^{-1} had the lowest ND values throughout, while the 60 kg N ha^{-1} plot had some spots with the highest ND values in certain locations. These patterns suggest interactions of N rates with soil heterogeneity (Mittermayer et al., 2021).

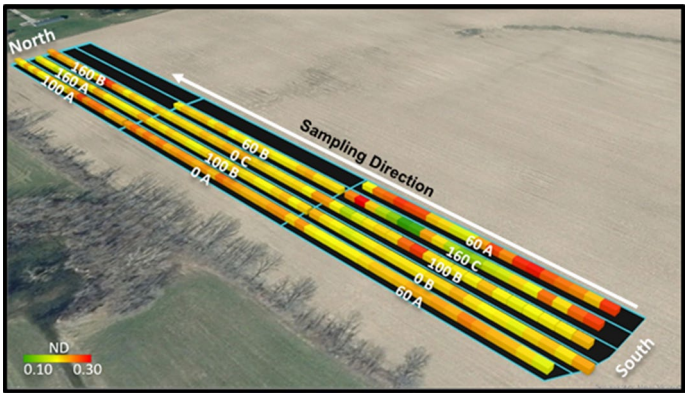

Fig. 14 ND index (R-B)/(R+B) value distribution response to applied N rates in Covington NY-2022. Based on 6.0-m averaged values

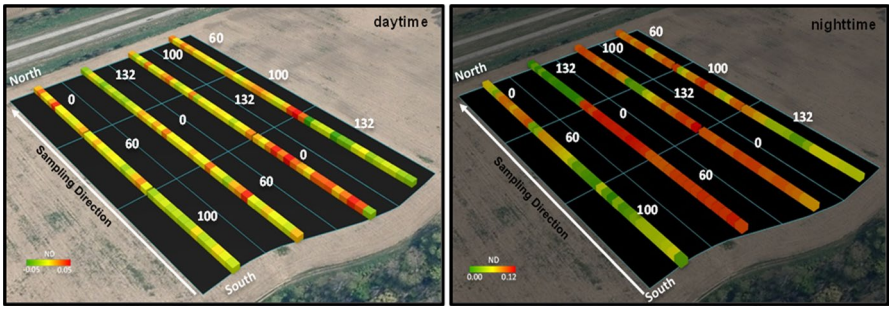

Fig. 15 Relationships between (R-B)/(R+B) based ND index and applied N rates (0, 60, 96, 132 N kg ha^{-1} in Geneseo NY-2022 based on 6.0-m averaged values

Geneseo, NY –2022

Figure 15 presents the distribution of the ND index means for different applied N rates in both daytime and nighttime measurements at the Geneseo site at 6-m resolution. The map highlights similarities and differences between the illumination conditions. As previously noted, both daytime and nighttime ND values tended to decrease as N rates increased, but considerable field variability was measured by the ND index. The nighttime imaging results generally exhibited more consistency and less field variability than the daytime measurements, but the pattern was consistent for both measurement times. Considering that nighttime imaging generally shows lower image-to-image variability, it is presumed that it also performs better at detecting field-scale variability at the 6-m resolution.

Conclusions

This study investigates the potential use of low-cost RGB cameras for detecting differences in pigment expression and maize nitrogen status at high spatial resolution using ground vehicle-based under-canopy imaging with the goal of variable-rate field N management. Significant correlations were measured between the (R-B)/(R+B) ratio and applied nitrogen rates for four trials in New York and Minnesota. Results also suggest the existence of considerable field-scale as well as site-specific variability that can be managed using under-canopy sensing with field robots. Hence, different fertilizer rates can be applied to small zones, and site-specific N applications can be managed with high accuracy with the proposed methodology. Normalized color intensity values based on the (R-B)/(R+B) index were different for daytime and nighttime imaging, and also varied in time, presumably due to effects from rainfall patterns. Nighttime imaging reduced image-to-image variability and generally improved correlations between the spectral ND index and N rate. (R-B)/(R+B) index values were generally consistent but were not able to determine whether other factors like differences in crop genotype and sensing time of day need to be accounted for. This suggests that, although the proposed approach is effective in identifying field variability patterns for N stress, its ability to accurately estimate an optimum N rate has not yet been established. Therefore, geo-referenced image data may be most effectively used in combination with other N rate estimators like dynamic simulation modeling. This level of precision in N application could potentially reduce the amount of excess fertilizer use and associated environmental impacts while improving crop productivity and profitability.

Appendix

See Appendix Tables 6, 7, 8; Fig. 16

Table 6 Soil and cropping information of experimental fields

	Minnesota 2019	Aurora, NY 2020	Geneseo, NY 2022	Covington, NY 2022
Planting date	20 MAY 2019	22 MAY 2020	26 MAY 2022	14 MAY 2022
Sampling date	DAP 59 (18 JULY)	DAP†54 (15 JULY), DAP60 (22 JULY), DAP66 (29 JULY)	DAP60 (24 JULY)	DAP72 (25 JUY)
Previous crop	Wheat	Continuous Maize	Small grain+legume	Maize
Soil	Silt Loam OM:2.8%	Silt Loam OM:3.9%	Silt Loam OM:1.9%	Gravelly silt loam OM:1.2%

DAP†: Day after planting

Table 7 Precipitation (P) and growing degree days (GDD) between April and August for each experimental site at 10- or 11-day increments

Field	Months	First 10 days		Second 10 days		Third 10 or 11 days		Total Month	
		P (mm)	GDD(°C)	P (mm)	GDD (C)	P (mm)	GDD (°C)	P (mm)	GDD (°C)
Minnesota 2019	April	11.9	11.4	81.8	10.6	18.2	36.9	111.9	58.9
	May	55.4	20.6	62.5	44.4	64.4	54.4	182.3	119.4
	June	29	105.8	12.2	79.7	39.7	110.8	80.9	296.4
	July	90.7	132.2	55.2	139.2	30.6	113.9	176.5	385.3
	August	8.2	121.4	53.3	110.6	39.8	84.4	101.3	316.4
	Total							**652.9**	**1176.0**
New York 2020	April	17.6	8.1	13.7	9.2	21.9	8.3	53.2	25.6
	May	63.2	18.9	35.6	35.3	12.7	100.0	111.5	154.2
	June	8.2	81.9	0.0	92.2	39.9	121.9	48.1	296.1
	July	3.1	135.3	89.0	131.1	51.8	138.1	143.9	404.4
	August	15.0	115.3	0.6	126.7	30.2	119.2	45.8	361.1
	Total							**402.5**	**1242.0**
New York 2022	April	5.4	50.0	14.2	65.3	23.6	64.4	43.2	53.6
	May	7.2	67.5	18.3	72.2	24.8	68.0	50.3	131.7
	June	35.3	69.3	46.8	66.4	0.5	79.7	82.6	247.2
	July	19.3	72.65	33.1	72.6	26.9	68.9	79.3	375.6
	August	4.8	60.85	13.3	77.3	48.3	59.5	66.4	322.2
	Total							**321.8**	**1014.4**

Table 8 Software and hardware used in the building process and their function

Hardware/software	Model and purpose	References
Motors	Model: IG42 24VDC 122 RPM 24VDC Reduction Ratio: 1:49 Rated Torque: 16 kgf-cm Rated Speed: 122 RPM Provides drive motion for wheels	(Shayang Ye, 2023)
Motor Mount Plate	1/8"thick aluminum plate to support motors M4 × 8 screws to mount the motor to the plate	(SuperDroid, 2023a, 2023b)
Electric Motor Hookup Kit	The kit includes capacitors, shielded wire, ferrite rings, and heat shrink	(SuperDroid, 2023a, 2023b)
Batteries	Model:12V 11Ah Lithium-Ion Phosphate Short Circuit Protection High Voltage Cut-Off Low Voltage Cut Off Cell Balancing Power source for control and motion systems	(K2Energy, 2022)
Heavy Duty Wheel and Shaft	Model: TD-164–010 Total Weight (set of wheels, shafts, collars, etc.): 8.6 lbs per set (4x)	(SuperDroid, 2023a, 2023b)
Motor Controller	Model: RoboClaw 2 × 30A Automatically supports 3.3V or 5 V logic levels, travel limit switches, home switches, emergency stop switches, power supplies, braking systems, and contactors	(Basicmicro, 2023)
transmitter & Receiver	Model: FLYSKY FS-i6X 2.4GHz Works in the frequency range of 2.405 to 2.475GHz Manual remote control	(Flysky, 2022)
Autodesk Inventor Pro2022	Model: Pro2022 The robot mechanical design, structure, and simulations	(Autodesk, 2022)
Blender	Version: 3.0 Rendering simulations	(Blender, 2022)
Proteus	Version: 8.15 Electrical system simulation	(Proteus, 2022)
Visual Studio	Version: 2022, Build Tools v143 Programming environment	(Microsoft, 2022a, 2022b)
Android Studio	Version: Chipmunk Driving view stream	(Google, 2022a, 2022b)
Arduino IDE	Version: 1.8.19 Robot driving system	(Arduino, 2021)
Raspberry Pi OS	Version: Debian-based, 32-bit, Bullseye Robot driving system and camera system	(Microsoft, 2022a, 2022b)
Firebases by Google	Version: Firestore v9 Realtime Database, Web-based control	(Google, 2022a, 2022b)
Camtasia Studio	Version: 2022.1 Interactive live video formats	(TechSmith, 2022)
Mapbox	Geolocation in live	(Mapbox, 2022)

Fig. 16 The thresholding method: **a** Original image taken with GoProHero7Black, **b** sky-masked image, **c** soil and sky masked image used to obtain average RGB digital numbers

Supplementary Information The online version contains supplementary material available at https://doi.org/10.1007/s11119-025-10262-0.

Acknowledgements The author acknowledges the financial support provided by the Graduate Education Scholarship (YLSY), which is a scholarship program offered by the Turkish Ministry of National Education.

Author contributions Zafer Bestas: Conceptualization, Methodology, Coding, Investigation, Visualization, Writing. Harold van Es: Conceptualization, Methodology, Writing—review editing, Visualization, Supervision. Kent Cavender-Bares: Field experimentation, Review, Advice. Bill Philpot: Review, Advice. David G. Rossiter: Review, Advice.

Data availability The datasets generated and analysed during the current study are not publicly available due to ongoing research developments, but are available from the corresponding author on reasonable request.

Declarations

Competing interest The authors declare that they have no known competing financial interests or personal relationships that could have appeared to influence the work reported in this paper.

References

Abit, M. J. M., Arnall, D. B., & Phillips, S. B. (2018). Environmental implications of precision agriculture. *Precision Agriculture Basics*. https://doi.org/10.2134/PRECISIONAGBASICS.2017.0035

Ahmad, I. S., & Reid, J. F. (1996). Evaluation of colour representations for maize images. *Journal of Agricultural Engineering Research, 63*(3), 185–195. https://doi.org/10.1006/JAER.1996.0020

Alivernini, A., Fares, S., Ferrara, C., & Chianucci, F. (2018). An objective image analysis method for estimation of canopy attributes from digital cover photography. *Trees - Structure and Function, 32*(3), 713–723. https://doi.org/10.1007/S00468-018-1666-3/FIGURES/4

Anderson, H. B., Nilsen, L., Tømmervik, H., Karlsen, S. R., Nagai, S., & Cooper, E. J. (2016). Using ordinary digital cameras in place of near-infrared sensors to derive vegetation indices for phenology studies of High Arctic vegetation. *Remote Sensing, 8*(10), 847. https://doi.org/10.3390/rs8100847

Arduino. (2021). *Arduino IDE (Version 1.8.19)* [Computer software]. https://www.arduino.cc/

Arduino. (2023). *Arduino Mega 2560 Rev3* [Electronic device]. https://store.arduino.cc/products/arduino-mega-2560-rev3

Arnold, J. B. (2021). *Extra Themes, Scales and Geoms for "ggplot2" [R package ggthemes version 4.2.4]*. https://CRAN.R-project.org/package=ggthemes

Autodesk. (2022). *Autodesk Inventor Pro 2022* [Computer software]. https://www.autodesk.com/

Bajwa, S., Tian, L. F., Gopalapillai, S., Tian, L., & Beal, J. (1999). Detection Of Nitrogen Stress In Corn Using Digital Aerial Imaging. https://www.researchgate.net/publication/2829250

Basicmicro. (2023). *RoboClaw 2x30A motor controller* [Electronic device]. https://www.basicmicro.com/

Ben-Shachar, M., Lüdecke, D., & Makowski, D. (2022). Indices of effect size [R package effect size version 0.8.2]. *Journal of Open Source Software, 5*(56), 2815. https://doi.org/10.21105/JOSS.02815

Bestas, Z., van Es, H., Cavender-Bares, K., & Philpot, W. D. (2025). Image-based quantification of leaf pigment variation in maize for early nitrogen stress detection. Manuscript submitted for publication.

Blender. (2022). *Blender (Version 3.0)* [Computer software]. https://www.blender.org/

Brodersen, C. R., & Vogelmann, T. C. (2010). Do changes in light direction affect absorption profiles in leaves? *Functional Plant Biology, 37*(5), 403–412. https://doi.org/10.1071/FP09262

Cai, Y., Guan, K., Nafziger, E., Chowdhary, G., Peng, B., Jin, Z., Wang, S., & Wang, S. (2019). Detecting in-season crop nitrogen stress of corn for field trials using UAV-and cubesat-based multispectral sensing. *IEEE Journal of Selected Topics in Applied Earth Observations and Remote Sensing, 12*(12), 5153–5166. https://doi.org/10.1109/JSTARS.2019.2953489

Campolo, J., Ortiz-Monasterio, I., Guerena, D., & Lobell, D. B. (2022). Evaluating maize yield response to fertilizer and soil in Mexico using ground and satellite approaches. *Field Crops Research, 276*, Article 108393. https://doi.org/10.1016/J.FCR.2021.108393

Chen, P., & Wang, F. (2022). Effect of crop spectra purification on plant nitrogen concentration estimations performed using high-spatial-resolution images obtained with unmanned aerial vehicles. *Field Crops Research, 288*, Article 108708. https://doi.org/10.1016/J.FCR.2022.108708

Correndo, A. A., Rotundo, J. L., Tremblay, N., Archontoulis, S., Coulter, J. A., Ruiz-Diaz, D., Franzen, D., Franzluebbers, A. J., Nafziger, E., Schwalbert, R., Steinke, K., Williams, J., Messina, C. D., & Ciampitti, I. A. (2021). Assessing the uncertainty of maize yield without nitrogen fertilization. *Field Crops Research, 260*, Article 107985. https://doi.org/10.1016/J.FCR.2020.107985

Davies, B., Coulter, J. A., & Pagliari, P. H. (2020). Timing and rate of nitrogen fertilization influence maize yield and nitrogen use efficiency. *PLoS ONE, 15*(5), Article e0233674. https://doi.org/10.1371/JOURNAL.PONE.0233674

Demetriades-Shah, T. H., & Court, M. N. (1987). International Journal of Remote Sensing Oblique view reflectance for assessing nitrogen status of incomplete canopies. *International Journal of Remote Sensing, 8*(7), 1049–1055. https://doi.org/10.1080/01431168708954747

Dong, R., Miao, Y., Wang, X., Chen, Z., Yuan, F., Zhang, W., & Li, H. (2020). Estimating plant nitrogen concentration of maize using a leaf fluorescence sensor across growth stages. *Remote Sensing*. https://doi.org/10.3390/rs12071139

Dutta, M. K., Singh, A., & Ghosal, S. (2015). A computer vision based technique for identification of acrylamide in potato chips. *Computers and Electronics in Agriculture, 119*, 40–50. https://doi.org/10.1016/j.compag.2015.10.007

Esri. (2021). *ArcGIS Pro Geostatistical Analyst Wizard (Version 3.0.1)* [Computer software]. Environmental Systems Research Institute. https://www.esri.com/en-us/arcgis/products/arcgis-pro/overview

Fan, J., Zhou, J., Wang, B., de Leon, N., Kaeppler, S. M., Lima, D. C., & Zhang, Z. (2022). Estimation of maize yield and flowering time using multi-temporal UAV-based hyperspectral data. *Remote Sensing, 14*(13), 3052. https://doi.org/10.3390/RS14133052

Flysky. (2022). *FS-i6X 2.4GHz 10CH transmitter and receiver* [Electronic device]. https://www.flysky-cn.com/

Geng, J., Liu, J., Kong, X., Shen, B., & Niu, Z. (2022). The fishmeal adulteration identification based on microscopic image and deep learning. *Computers and Electronics in Agriculture*. https://doi.org/10.1016/j.compag.2022.106974

Gilliot, J. M., Michelin, J., Hadjard, D., & Houot, S. (2021). An accurate method for predicting spatial variability of maize yield from UAV-based plant height estimation: A tool for monitoring agronomic field experiments. *Precision Agriculture, 22*(3), 897–921. https://doi.org/10.1007/S11119-020-09764-W/FIGURES/16

Google. (2022). *Android Studio Chipmunk (2022)* [Computer software]. https://developer.android.com/studio

Google. (2022). *Firebase Firestore v9* [Web service]. https://firebase.google.com/

Griffin, T. W., Shockley, J. M., & Mark, T. B. (2018). Economics of precision farming. *Precision Agriculture Basics*. https://doi.org/10.2134/PRECISIONAGBASICS.2016.0098

Harvey, P. (2022). *ExifTool (Version 12.42)* [Computer software]. https://exiftool.org/

He, J., Zhang, X., Guo, W., Pan, Y., Yao, X., Cheng, T., Zhu, Y., Cao, W., & Tian, Y. (2020). Estimation of vertical leaf nitrogen distribution within a rice canopy based on hyperspectral data. *Frontiers in Plant Science, 10*, Article 498767. https://doi.org/10.3389/FPLS.2019.01802/BIBTEX

K2 Energy. (2022). *12V 11Ah LiFePO4 battery* [Battery datasheet]. https://www.k2battery.com/

Liu, W., Liu, G., Yang, Y., Guo, X., Ming, B., Xie, R., Liu, Y., Wang, K., Hou, P., & Li, S. (2021). Spatial variation of maize height morphological traits for the same cultivars at a large agroecological scale. *European Journal of Agronomy, 130*, Article 126349. https://doi.org/10.1016/J.EJA.2021.126349

Mamo, M., Malzer, G. L., Mulla, D. J., Huggins, D. R., & Strock, J. (2003). Spatial and temporal variation in economically optimum nitrogen rate for corn. *Agronomy Journal, 95*(4), 958–964. https://doi.org/10.2134/AGRONJ2003.9580

Mapbox. (2022). *Mapbox API* [Geolocation platform]. https://www.mapbox.com/

Melkonian, J.J., van Es, H.M., De Gaetano, A.T., & Joseph, L. 2008. ADAPT-N: Adaptive nitrogen management for maize using high-resolution climate data and model simulations. In R. Kosla, (Ed.), *Proceedings of the 9th International Conference on Precision Agriculture*, Denver, CO. 20–23 July 2008. Colorado State Univ.

Melkonian, J., Poffenbarger, H. J., Mirsky, S. B., Ryan, M. R., & Moebius-Clune, B. N. (2017). Estimating nitrogen mineralization from cover crop mixtures using the precision nitrogen management model. *Agronomy Journal, 109*(5), 1944–1959. https://doi.org/10.2134/AGRONJ2016.06.0330

Microsoft. (2022a). *Raspberry Pi OS (Bullseye, 32-bit)* [Operating system]. https://www.raspberrypi.com/software

Microsoft. (2022b). *Visual Studio 2022, Build Tools v143* [Computer software]. https://visualstudio.microsoft.com/

Mittermayer, M., Gilg, A., Maidl, F.-X., Nätscher,·L., & Hülsbergen, K.-J. (2021). *Site-specific nitrogen balances based on spatially variable soil and plant properties*. *22*, 1416–1436. https://doi.org/10.1007/s11119-021-09789-9

Ogunboye, O. I., Adekiya, A. O., Ewulo, B. S., & Olayanju, A. (2020). Effects of split application of urea fertilizer on soil chemical properties, maize performance and profitability in Southwest Nigeria. *The Open Agriculture Journal, 14*(1), 36–42. https://doi.org/10.2174/1874331502014010036

Pagola, M., Ortiz, R., Irigoyen, I., Bustince, H., Barrenechea, E., Aparicio-Tejo, P., Lamsfus, C., & Lasa, B. (2009). New method to assess barley nitrogen nutrition status based on image colour analysis: Comparison with SPAD-502. *Computers and Electronics in Agriculture, 65*(2), 213–218. https://doi.org/10.1016/J.COMPAG.2008.10.003

Pasuquin, J. M., Pampolino, M. F., Witt, C., Dobermann, A., Oberthür, T., Fisher, M. J., & Inubushi, K. (2014). Closing yield gaps in maize production in Southeast Asia through site-specific nutrient management. *Field Crops Research, 156*, 219–230. https://doi.org/10.1016/J.FCR.2013.11.016

Patil, I., Makowski, D., Ben-Shachar, M. S., Wiernik, B. M., Bacher, E., & Lüdecke, D. (2022). datawizard: An R Package for easy data preparation and statistical transformations. *Journal of Open Source Software, 7*(78), 4684. https://doi.org/10.21105/JOSS.04684

Plett, D. C., Ranathunge, K., Melino, V. J., Kuya, N., Uga, Y., & Kronzucker, H. J. (2020). The intersection of nitrogen nutrition and water use in plants: New paths toward improved crop productivity. *Journal of Experimental Botany, 71*(15), 4452–4468. https://doi.org/10.1093/JXB/ERAA049

Prey, L., & Schmidhalter, U. (2019). Simulation of satellite reflectance data using high-frequency ground based hyperspectral canopy measurements for in-season estimation of grain yield and grain nitrogen status in winter wheat. *ISPRS Journal of Photogrammetry and Remote Sensing, 149*, 176–187. https://doi.org/10.1016/j.isprsjprs.2019.01.023

Proteus. (2022). *Proteus Design Suite (Version 8.15)* [Simulation software]. https://www.labcenter.com/

Putra, B. T. W., & Soni, P. (2020). Improving nitrogen assessment with an RGB camera across uncertain natural light from above-canopy measurements. *Precision Agriculture, 21*(1), 147–159. https://doi.org/10.1007/S11119-019-09656-8/FIGURES/7

R Core Team. (2022). *R: A language and environment for statistical computing (Version 4.2.2)* [Computer software]. R Foundation for Statistical Computing. https://www.R-project.org/

Ribaudo, M., Delgado, J., Hansen, L., Livingston, M., Mosheim, R., & Williamson, J. (2011). United States Department of Agriculture Economic Research Service Nitrogen in Agricultural Systems: Implications for Conservation Policy Economic Research Report Number 127. https://www.ers.usda.gov/briefing/agchemicals/

Sakamoto, T., Shibayama, M., Takada, E., Lnoue, A., Morita, K., Takahashl, W., Miura, S., & Kimura, A. (2010). Detecting seasonal changes in crop community structure using day and night digital images. *Photogrammetric Engineering and Remote Sensing, 76*(6), 713–726. https://doi.org/10.14358/PERS.76.6.713

Sela, S., van Es, H. M., Moebius-Clune, B. N., Marjerison, R., Melkonian, J., Moebius-Clune, D., Schindelbeck, R., & Gomes, S. (2016). Adapt-N outperforms grower-selected nitrogen rates in Northeast and Midwestern United States strip trials. *Agronomy Journal, 108*(4), 1726–1734. https://doi.org/10.2134/agronj2015.0606

Shannon, D. K., Clay, D. E., & Sudduth, K. A. (2018). An introduction to precision agriculture. *Precision Agriculture Basics*. https://doi.org/10.2134/PRECISIONAGBASICS.2016.0084

Sharifi, A. (2020). Using sentinel-2 data to predict nitrogen uptake in maize crop. *IEEE Journal of Selected Topics in Applied Earth Observations and Remote Sensing, 13*, 2656–2662. https://doi.org/10.1109/JSTARS.2020.2998638

Shaver, T. M., Khosla, R., & Westfall, D. G. (2010). Evaluation of two ground-based active crop canopy sensors in maize: Growth stage, row spacing, and sensor movement speed. *Soil Science Society of America Journal, 74*(6), 2101–2108. https://doi.org/10.2136/sssaj2009.0421

Shayang Ye. (2023). *IG42 24VDC 122 RPM gear motor* [Technical specification]. http://www.shayangye.com/

Shi, P., Wang, Y., Xu, J., Zhao, Y., Yang, B., Yuan, Z., & Sun, Q. (2020). Rice nitrogen nutrition estimation with RGB images and machine learning methods. *Computers and Electronics in Agriculture*. https://doi.org/10.1016/j.compag.2020.105860

Sogbedji, J. M., van Es, H. M., Klausner, S. D., Bouldin, D. R., & Cox, W. J. (2001). Spatial and temporal processes affecting nitrogen availability at the landscape scale. *Soil and Tillage Research, 58*(3–4), 233–244. https://doi.org/10.1016/S0167-1987(00)00171-9

Stamatiadis, S., Taskos, D., Tsadila, E., Christofides, C., Tsadilas, C., & Schepers, J. S. (2010). Comparison of passive and active canopy sensors for the estimation of vine biomass production. *Precision Agriculture, 11*(3), 306–315. https://doi.org/10.1007/s11119-009-9131-3

SuperDroid. (2023). *Motor mount plate and hookup kit* [Mechanical accessory]. https://www.superdroidrobots.com/

SuperDroid. (2023). *TD-164–010 Heavy Duty Wheels and Shafts* [Mechanical components]. https://www.superdroidrobots.com/

TechSmith. (2022). *Camtasia Studio (Version 2022.1)* [Computer software]. https://www.techsmith.com/

Tremblay, N., Wang, Z., Ma, B. L., Belec, C., & Vigneault, P. (2009). A comparison of crop data measured by two commercial sensors for variable-rate nitrogen application. *Precision Agriculture, 10*(2), 145–161. https://doi.org/10.1007/s11119-008-9080-2

van Es, H. M., Gomes, C. P., Sellmann, M., & van Es, C. L. (2007a). Spatially-Balanced Complete Block designs for field experiments. *Geoderma, 140*(4), 346–352. https://doi.org/10.1016/J.GEODERMA.2007.04.017

van Es, H. M., Kay, B. D., Melkonian, J. J., & Sogbedji, J. M. (2007b). Nitrogen management under maize in humid regions: Case for a dynamic approach. In T. Bruulsema (Ed.), *Managing crop nutrition for weather* (pp. 6–13). Plant Nutrition Institute Publ.

Virtanen, O., Constantinidou, E., & Tyystjärvi, E. (2022). Chlorophyll does not reflect green light–how to correct a misconception. *Journal of Biological Education, 56*(5), 552–559. https://doi.org/10.1080/00219266.2020.1858930

Wang, Z., Chen, J., Zhang, J., Tan, X., Ali Raza, M., Ma, J., Zhu, Y., Yang, F., & Yang, W. (2022). Assessing canopy nitrogen and carbon content in maize by canopy spectral reflectance and uninformative variable elimination. *The Crop Journal, 10*(5), 1224–1238. https://doi.org/10.1016/J.CJ.2021.12.005

Wickham, H. (2016). *ggplot2: Elegant graphics for data analysis*. https://ggplot2.tidyverse.org/

Winterhalter, L., Mistele, B., & Schmidhalter, U. (2012). Assessing the vertical footprint of reflectance measurements to characterize nitrogen uptake and biomass distribution in maize canopies. *Field Crops Research, 129*, 14–20. https://doi.org/10.1016/j.fcr.2012.01.007

WSS. (2022). Retrieved December 5, 2022, from https://websoilsurvey.sc.egov.usda.gov/App/WebSoilSurvey.aspx

Wu, Y., Li, Q., Jin, R., Chen, W., Liu, X., Kong, F., Ke, Y., Shi, H., & Yuan, J. (2019). Effect of low-nitrogen stress on photosynthesis and chlorophyll fluorescence characteristics of maize cultivars with different low-nitrogen tolerances. *Journal of Integrative Agriculture, 18*(6), 1246–1256. https://doi.org/10.1016/S2095-3119(18)62030-1

Xiao, Y., Tholen, D., & Zhu, X. G. (2016). The influence of leaf anatomy on the internal light environment and photosynthetic electron transport rate: Exploration with a new leaf ray tracing model. *Journal of Experimental Botany, 67*(21), 6021–6035. https://doi.org/10.1093/JXB/ERW359

Xiong, N. N., Shen, Y., Yang, K., Lee, C., & Wu, C. (2018). Color sensors and their applications based on real-time color image segmentation for cyber physical systems. *Eurasip Journal on Image and Video Processing, 2018*(1), 1–16. https://doi.org/10.1186/S13640-018-0258-X/FIGURES/6

Xue, L., Cao, W., Luo, W., Dai, T., & Zhu, Y. (2004). Monitoring leaf nitrogen status in rice with canopy spectral reflectance. *Agronomy Journal, 96*(1), 135–142. https://doi.org/10.2134/agronj2004.0135

Xu, X., Fan, L., Li, Z., Meng, Y., Feng, H., Yang, H., & Xu, B. (2021). Estimating leaf nitrogen content in corn based on information fusion of multiple-sensor imagery from UAV. *Remote Sensing, 13*(3), 1–17. https://doi.org/10.3390/rs13030340

Yadav, S. P., Ibaraki, Y., & Gupta, S. D. (2010). Estimation of the chlorophyll content of micropropagated potato plants using RGB based image analysis. *Plant Cell, Tissue and Organ Culture, 100*(2), 183–188. https://doi.org/10.1007/S11240-009-9635-6

Yates, S. R., spsampsps Warrick, A. W. (2002). Geostatistics. In J. H. Dane, spsampsps G. C. Topp (Eds.), *Methods of Soil Analysis: Part 4—Physical Methods* (pp. 81–118). Soil Science Society of America. https://doi.org/10.2136/sssabookser5.4.c4

Yue, J., Guo, W., Yang, G., Zhou, C., Feng, H., & Qiao, H. (2021). Method for accurate multi-growth-stage estimation of fractional vegetation cover using unmanned aerial vehicle remote sensing. *Plant Methods*. https://doi.org/10.1186/S13007-021-00752-3

Zhang, J., Sun, H., Gao, D., Qiao, L., Liu, N., Li, M., & Zhang, Y. (2020). Detection of canopy chlorophyll content of corn based on continuous wavelet transform analysis. *Remote Sensing*. https://doi.org/10.3390/RS12172741

Authors and Affiliations

Zafer Bestas[1] · Harold M. van Es[1] · William D. Philpot[2] · Kent Cavender-Bares[3] · David G. Rossiter[1,4]

✉ Zafer Bestas
zb48@cornell.edu

Harold M. van Es
hmv1@cornell.edu

William D. Philpot
wdp2@cornell.edu

Kent Cavender-Bares
kbares@rowbot.com

David G. Rossiter
d.g.rossiter@cornell.edu

[1] Section of Soil and Crop Sciences, School of Integrative Plant Science, Cornell University, Ithaca, NY 14853, USA

[2] School of Civil and Environmental Engineering, Cornell University, Ithaca, NY 14850, USA

[3] Rowbot Systems, St Paul, MN, USA

[4] ISRIC-World Soil Information, 6700 AJ Wageningen, The Netherlands